Directional multiscale processing of images using wavelets with composite dilations

Glenn R. Easley *

System Planning Corporation, Arlington, VA

Demetrio Labate

Department of Mathematics, University of Houston, Houston, TX 77204, USA

Vishal M. Patel

University of Maryland, College Park, MD 20742

Abstract

It is widely recognized that the performance of many image processing algorithms can be significantly improved by applying multiscale image representations with the ability to handle very efficiently directional and other geometric features. *Wavelets with composite dilations* offer a flexible and especially effective framework for the construction of such representations. Unlike traditional wavelets, this approach enables the construction of waveforms ranging not only over various scales and locations but also over various orientations and other orthogonal transformations. Several useful constructions are derived from this approach, including the well-known shearlet representation and new ones, introduced in this paper. In this work, we introduce and apply a novel multiscale image decomposition algorithm for the efficient digital implementation of wavelets with composite dilations. Due to its ability to handle geometric features efficiently, our new image processing algorithms provides consistent improvements upon competing state-of-the-art methods, as illustrated on a number of image denoising and image enhancement demonstrations.

Key words: Wavelets, directional filter banks, wavelets with composite dilations, contourlets, shearlets, curvelets.

* Corresponding author
Email addresses: geasley@sysplan.com (Glenn R. Easley), dlabate@math.uh.edu (Demetrio Labate), pvishalm@umiacs.umd.edu (Vishal M. Patel).

1 Introduction

It has become commonly understood that while 1D wavelets are optimal at approximating point singularities, their 2D separable counterparts are not equally effective at approximating singularities along curves which model edges in images. The need for directional filtering in order to improve multidimensional data processing was early recognized, for example, in the works [1,22,39]. More recently, new generations of directional representations were developed which exhibit near optimal approximations on the class of cartoon images. The most notable of these representations are the *curvelets* [40,7], the *contourlets* [12] and the *shearlets* [25,33], which are constructed by defining systems of analyzing waveforms ranging not only at various scales and locations, like traditional wavelets, but also at various orientations, with the number of orientations increasing at finer scales.

Within the context of improved multidimensional representations, the theory of *wavelets with composite dilations*, originally developed in [25–27], are especially important. This framework is a generalization of the classical theory from which traditional wavelets are derived, and it provides a very flexible setting for the construction of many truly multidimensional variants of wavelets, such as the well known construction of shearlets, which was mentioned above. Several additional sophisticated constructions using this approach were obtained by Blanchard [4,5], by Kryshtal and Blanchard in a paper which exploits the connection with crystallographic groups [6], and by Kryshtal et al. [31]. Furthermore, it was recently shown by two of the authors in [15] that several recent filter bank constructions such as the hybrid wavelets of Eslami and Rada [19–21] and the variants of the contourlets construction proposed in [30,43] can either be derived or are closely related to systems obtained from the framework of wavelets with composite dilations.

These results illustrate the potential of wavelets with composite dilations for the construction of directional multiscale representations going far beyond traditional wavelets with respect to their ability to represent geometric features. However, except for some very special cases, no satisfactory method for designing efficient numerical implementations of wavelets with composite dilations was developed so far, due to the difficulty of adapting the standard wavelet implementation algorithms to this more general setting. The goal of this paper is to introduce a new general procedure for the design of discrete multiscale transforms which takes full advantage of the geometric features associated with the framework of wavelets with composite dilations. Using this approach, we are able to design and implement several new classes of directional *discrete* transforms and to obtain improved implementations of known ones. As will be illustrated in this paper, the newly derived algorithms based on wavelets with composite dilations are highly competitive in imaging applications such

as denoising and enhancement.

Recall that, for tasks such as image denoising and enhancement, where the objective is to extract or emphasize certain image features, it is often beneficial to use redundant representations. A standard method for designing nonsubsampled directional representations is to use critically sampled transformations in combination with resampling operations (i.e., [11,21]). As will become clear below, this approach is frequently associated with filters that do not faithfully match with the desired theoretical spatial-frequency decomposition. By contrast, in this paper we introduce a novel filter bank construction technique that enables the projection of the data directly onto the desired directionally-oriented frequency subbands. A key new feature of our construction is the ability to generate the transform coefficients by directly applying the action of the matrices associated with the spatial-frequency decomposition. This is in contrast to earlier implementations such as the discrete shearlet transform in [16], which was designed to mimic the desired spatial-frequency decomposition. Not only our new approach follows directly from the theoretical setting, but it also allows for more sophisticated composite wavelet decompositions enabling a much finer handling of the geometry in the data. As special cases of our approach, we obtain an improved implementation of the shearlet transform and we introduce new *hyperbolic* composite wavelet transforms. The last transforms, in particular, have potentially high impact in deconvolution and other image enhancement applications, as indicated by the novel decompositions suggested in [9] and by the techniques for dealing with motion blur recently proposed in [18].

1.1 Paper Organization

The definition and basic properties of wavelets with composite dilations, along with several novel constructions are presented in Section 2. Their novel discrete implementation procedures are discussed in Section 3. Numerical demonstrations illustrating the performance of the new constructions for denoising and image enhancement are presented in Section 4. Finally, concluding remarks are given in Section 5.

2 Wavelets with composite dilations

Let us introduce the notation which will be used subsequently. Given $\tau \in \mathbb{R}^n$, the *translation operator* T_τ on $L^2(\mathbb{R}^n)$ is defined by

$$T_\tau f(x) = f(x - \tau), \quad x \in \mathbb{R}^n, \quad f \in L^2(\mathbb{R}^n).$$

For $a \in GL_n(\mathbb{R})$ (where $GL_n(\mathbb{R})$ denotes the group of invertible matrices on $\mathbb{R}^n$), the *dilation operator* D_a is given by

$$D_a f(x) = |\det a|^{-1/2} f(a^{-1}x).$$

We adopt the convention that the points $x \in \mathbb{R}^n$ are column vectors, while the points $\xi \in \widehat{\mathbb{R}}^n$ (the Fourier domain) are row vectors. Hence a vector x multiplying a matrix $a \in GL_n(\mathbb{R})$ on the right is a column vector and a vector ξ multiplying a matrix $a \in GL_n(\mathbb{R})$ on the left is a row vector; that is, $ax \in \mathbb{R}^n$ and $\xi a \in \widehat{\mathbb{R}}^n$. The Fourier transform of $f \in L^2(\mathbb{R}^n)$ is given by

$$\hat{f}(\xi) = \int_{\mathbb{R}^n} f(x)\, e^{2\pi i \xi \cdot x}\, dx,$$

where $\xi \in \widehat{\mathbb{R}}^n$ and the inverse Fourier transform is

$$\check{f}(x) = \int_{\widehat{\mathbb{R}}^n} f(\xi)\, e^{-2\pi i \xi \cdot x}\, d\xi.$$

The standard *wavelet systems* generated by $\Psi = \{\psi_1, \ldots, \psi_L\} \subset L^2(\mathbb{R}^n)$ and $A = \{a^i : i \in \mathbb{Z}\}$ are the collections of functions of the form

$$\{D_a^j\, T_k\, \psi_m : j \in \mathbb{Z}, k \in \mathbb{Z}^n, m = 1, \ldots, L\},$$

which form a Parseval frame for $L^2(\mathbb{R}^n)$. That is, for all $f \in L^2(\mathbb{R}^n)$, the following expansion formula [1] holds:

$$\|f\|^2 = \sum_{j \in \mathbb{Z}} \sum_{k \in \mathbb{Z}^n} |\langle f, D_a^j\, T_k\, \Psi \rangle|^2.$$

Note that the traditional wavelet systems are obtained with $a = 2\,I$, where I is the identity matrix. That is, the dilation factor is the same for all coordinate axes.

The *wavelets with composite dilations* [25] overcome the limitations of standard wavelets in dealing with the geometry of multivariate functions by including a second set of dilations. Namely, they have the form

$$\mathcal{A}_{AB}(\Psi) = \{D_a D_b\, T_k\, \Psi :\ k \in \mathbb{Z}^n,\ a \in A,\ b \in B\},$$

where A, B are countable subsets of $GL_n(\mathbb{R})$ and the matrices $b \in B$ satisfy $|\det b| = 1$. Analogous to standard wavelet systems, $\Psi \subset L^2(\mathbb{R}^n)$ is chosen so that

$$\|f\|^2 = \sum_{a \in A} \sum_{b \in B} \sum_{k \in \mathbb{Z}^n} |\langle f, D_a\, D_b\, T_k \Psi \rangle|^2,$$

[1] Recall that an orthonormal basis is a special case of a Parseval frame; however, the elements of a Parseval frame need not be orthogonal.

for any $f \in L^2(\mathbb{R}^n)$. Usually, the matrices $a \in A$ are expanding (but not necessarily isotropic, as in the traditional wavelet case); the matrices $b \in B$, which are non-expanding, are associated with rotations and other orthogonal transformations. As a result, one can define systems of wavelets with composite dilations containing elements that are "long and narrow" and range over many locations, scales, shapes and directions. As mentioned above, a particularly prominent example of wavelets with composite dilations is the shearlet system, which provides a nearly optimally sparse representation for a general class of images and other high dimensional data [23,24]. Several additional examples will be described below.

The theory of wavelets with composite dilations extends nicely many of the standard results of wavelet theory (see [25–27]) and, at the same time, it allows for a much richer directionality in its representation. In particular, it is rather straightforward to obtain the following simple conditions for the constructions of wavelets with composite dilations in the case where the generator ψ is chosen such that $\hat{\psi} = \chi_S$, where $S \subset \mathbb{R}^2$ and χ_S denotes the characteristic function of S. Although the result below holds in any dimension, we state it in dimension $n = 2$ since this will be the situation considered in the rest of the paper.

Theorem 1 *Let A, B be subsets of $GL_2(\mathbb{R})$ and $S \subset F \subset \mathbb{R}^2$. Suppose that the following conditions hold:*

(1) $\widehat{\mathbb{R}}^2 = \bigcup_{k\in\mathbb{Z}^2}(F + k)$,
(2) $\widehat{\mathbb{R}}^2 = \bigcup_{a\in A, b\in B} S\,(ab)^{-1}$,

where the unions are disjoint up to a set of measure zero. Then for $\psi = (\chi_S)^\vee$ the system $\mathcal{A}_{AB}$ is a Parseval frame for $L^2(\mathbb{R}^2)$. If, in addition, $\|\psi\| = 1$, then $\mathcal{A}_{AB}$ is an orthonormal basis for $L^2(\mathbb{R}^2)$.

Hence, in analogy to the wavelet case, $\mathcal{A}_{AB}$ is a system of wavelets with composite dilations if the collections of A- and B-dilations of S form a tiling of the frequency plane.

It is clear that the systems described in Theorem 1 are not well-localized in the spatial domain, since their elements are characteristic functions of sets in the frequency domain and, hence, have slow spatial decay. Wavelets with composite dilations which are well-localized require ad hoc constructions such as the shearlets in [23] or the constructions described in [15]. Some additional new well-localized constructions are introduced in this paper.

2.1 Some Constructions

In this section, we apply Theorem 1 to construct several examples of wavelets with composite dilations for $L^2(\mathbb{R}^2)$. This is useful both to illustrate the variety of possible constructions which can be derived from this approach, and to set the groundwork for new discrete multiscale transforms which will be developed in Section 3. Notice that Constructions 1-3 are not new (see [26,27]), and are included for completeness and comparison. As indicated below, Constructions 1-2 are formally equivalent to systems recently introduced in the literature using an ad hoc construction, but they can be derived from the general framework of wavelets with composite dilations. More attention will be devoted to Construction 4, which is new.

2.1.1 Construction 1

Let $A = \{a^j : j \in \mathbb{Z}\}$ where $a = \left(\begin{smallmatrix} 1 & 1 \\ -1 & 1 \end{smallmatrix}\right)$ (the quincunx matrix) and consider $B = \{\pm b_0, \pm b_1, \pm b_2, \pm b_3\}$ where $b_0 = \left(\begin{smallmatrix} 1 & 0 \\ 0 & 1 \end{smallmatrix}\right)$, $b_1 = \left(\begin{smallmatrix} 1 & 0 \\ 0 & -1 \end{smallmatrix}\right)$, $b_2 = \left(\begin{smallmatrix} 0 & 1 \\ 1 & 0 \end{smallmatrix}\right)$, $b_3 = \left(\begin{smallmatrix} 0 & -1 \\ -1 & 0 \end{smallmatrix}\right)$. Notice that B is the group of symmetries of the square.

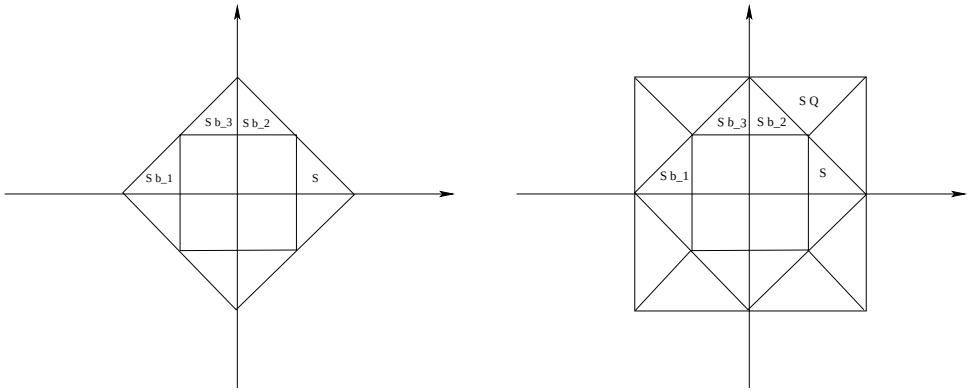

Fig. 1. *Tiling of the frequency domain associated with a system of wavelets with composite dilations, where a is the quincunx dilation matrix and B is the group of symmetries of the square.*

Let $\hat{\psi}(\xi) = \chi_S(\xi)$, where the set S is the union of the triangles with vertices $(1,0),(2,0),(1,1)$ and $(-1,0),(-2,0),(-1,-1)$, which is illustrated in Figure 1. A direct calculation shows that S satisfies the assumptions of Theorem 1, so that the system

$$\mathcal{A}_{AB}(\psi) = \{D_a^j\, D_b\, T_k\, \psi : \, j \in \mathbb{Z},\, b \in B,\, k \in \mathbb{Z}^2\}$$

is an orthonormal basis for $L^2(\mathbb{R}^2)$ (in fact, it is a Parseval frame and $\|\psi\| = 1$).

As noticed in [15], the frequency partition achieved by the Hybrid Quincunx Wavelet Directional Transform (HQWDT) from [21] is a simple modification

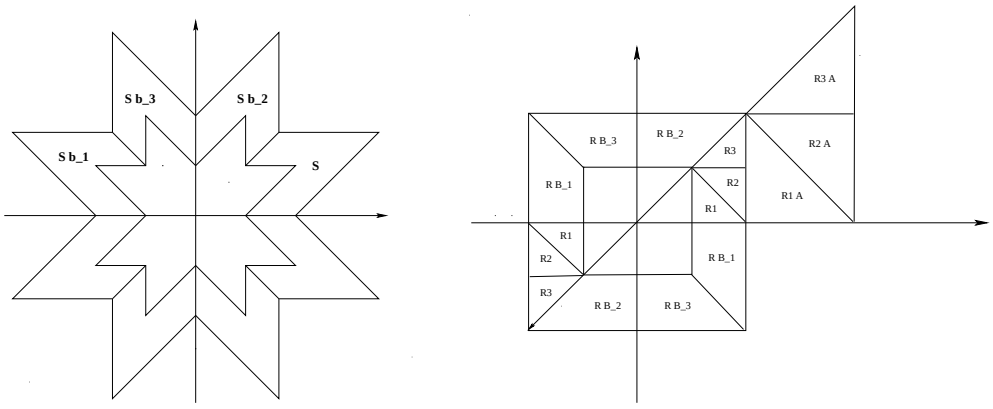

Fig. 2. *Left: tiling of the frequency domain associated with a system of wavelets with composite dilations where a is the quincunx dilation matrix and B is the group of symmetries of the square. Right: tiling of the frequency domain associated with a system of wavelets with composite dilations where* $a = 2I$ *and B is the group of symmetries of the square.*

of this construction, which is obtained by splitting each triangle of the set S into 2 smaller triangles. Another example, with the same matrices A and B, but a different generating set S, is illustrated in Figure 2 on the left. For future labeling, we will refer to this second construction concisely as the *ab-star* decomposition alluding to its star-like spatial-frequency tiling and its composite wavelet origin.

2.1.2 Construction 2

Let $A = \{a^j : j \in \mathbb{Z}\}$ where $a = \left(\begin{smallmatrix} 2 & 0 \\ 0 & 2 \end{smallmatrix}\right)$ and consider $B = \{b_0, b_1, b_2, b_3\}$ where $b_0 = \left(\begin{smallmatrix} 1 & 0 \\ 0 & 1 \end{smallmatrix}\right)$, $b_1 = \left(\begin{smallmatrix} 1 & 0 \\ 0 & -1 \end{smallmatrix}\right)$, $b_2 = \left(\begin{smallmatrix} 0 & 1 \\ 1 & 0 \end{smallmatrix}\right)$, $b_3 = \left(\begin{smallmatrix} 0 & -1 \\ -1 & 0 \end{smallmatrix}\right)$.

Let R be the union of the trapezoid with vertices $(1,0), (2,0), (1,1), (2,2)$ and the symmetric one with vertices $(-1,0), (-2,0), (-1,-1), (-2,-2)$. Next, we partition each trapezoid into right triangles R_m, $m = 1, 2, 3$, as illustrated in Figure 2 on the right. Hence we define $\Psi = \{\psi^m : m = 1, 2, 3\}$, where $\hat{\psi}^m(\xi) = \chi_{R_m}(\xi)$. Then the system

$$\mathcal{A}_{AB}(\Psi) = \{D_a^j \, D_b \, T_k \, \Psi : \, j \in \mathbb{Z}, \, b \in B, \, k \in \mathbb{Z}^2\}$$

is an orthonormal basis for $L^2(\mathbb{R}^2)$.

2.1.3 Construction 3.

Another example of a system of wavelets with composite dilations is obtained by keeping the same set A of dilation matrices as in Construction 2, and redefining B as the set $\{b^\ell : -3 \leq \ell \leq 2\}$, where b is the shear matrix $\left(\begin{smallmatrix} 1 & 1 \\ 0 & 1 \end{smallmatrix}\right)$. For

that, let R be the union of the trapezoid with vertices $(1,0),(2,0),(1,1/3),(2,2/3)$ and the symmetric one with vertices $(-1,0),(-2,0),(-1,-1/3),(-2,-2/3)$, $\tilde{R} = Rr$, where $r = \left(\begin{smallmatrix} 0 & 1 \\ -1 & 0 \end{smallmatrix}\right)$ and define $\Psi = \{\psi^m : m = 1,2\}$, where $\hat{\psi}^1 = \chi_R$, and $\hat{\psi}^2 = \chi_{\tilde{R}}$. It follows that the system

$$\mathcal{A}_{\mathcal{AB}}(\Psi) = \{D_a^j\, D_b\, T_k\, \Psi : j \in \mathbb{Z},\, b \in B,\, k \in \mathbb{Z}^2\}$$

is an orthonormal basis for $L^2(\mathbb{R}^2)$. For practical applications, it is useful to modify this system by restricting the scale parameter to the values $j \geq 0$ and by taking care of the low frequency region of the frequency plane using a standard wavelet basis. The frequency tiling corresponding to this system is illustrated in Figure 3. As observed in [15], this frequency tiling is similar to

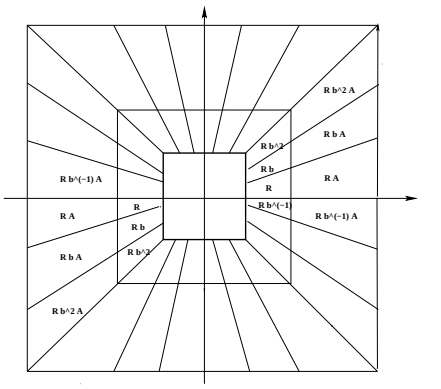

Fig. 3. *Tiling of the frequency domain associated with a system of wavelets with composite dilations where $a = 2I$ and B is the set of shearing matrices.*

the one used for the Non-Uniform Directional Filter Bank (NUDFB) in [36]. If this construction is combined with a separable generator, then one obtains the frequency tiling corresponding to the Hybrid Wavelet Directional Transform (HWDT) from [21] and to the directional filter bank construction used in [43].

2.2 Construction 4. Hyperbolic tiling

Another example of a system of wavelets with composite dilations is obtained by using a set of matrices of the form

$$B = \left\{ b_\ell = \begin{pmatrix} \lambda^{-\ell} & 0 \\ 0 & \lambda^{\ell} \end{pmatrix} : \ell \in \mathbb{Z} \right\}, \tag{1}$$

where $\lambda > 1$ is a fixed parameter [2]. As it will be clear from the analysis below, this construction can be seen as a transformation of the shearlet tiling under a nonlinear change of coordinates. In what follows, we will set $\lambda = \sqrt{2}$, but the discussion below can be easily extended to other choices of λ.

Let us start by noticing that, for each $k > 0$, the set $H_k = \{(\xi_1, \xi_2) \in \widehat{\mathbb{R}}^2 : \xi_1\xi_2 = k\}$ consists of two branches of hyperbolas. Observe that, for any $\xi = (\xi_1, \xi_2) \in H_k$, every other point ξ' on the same branch of the hyperbola has the unique representation $\xi' = (\xi_1\gamma^{-t}, \xi_2\gamma^t)$ for some $t \in \mathbb{R}$, where $\gamma > 1$ is fixed. In particular, any $\xi = (\xi_1, \xi_2)$ in quadrant I can be parametrized by

$$\xi(r, t) = (\sqrt{r}\,(\sqrt{2})^{-t}, \sqrt{r}\,(\sqrt{2})^t),$$

where $r \geq 0$, $t \in \mathbb{R}$. This implies that

$$r = \xi_1\,\xi_2, \quad 2^t = \frac{\xi_2}{\xi_1}.$$

For any $k_1 < k_2$, a set $\{\xi(r, t) : k_1 \leq r < k_2\}$ is a *hyperbolic strip* and, for $m_1 < m_2$, a set $\{\xi(r, t) : k_1 \leq r < k_2, m_1 \leq 2^t \leq m_2\}$ is a *hyperbolic trapezoid*.

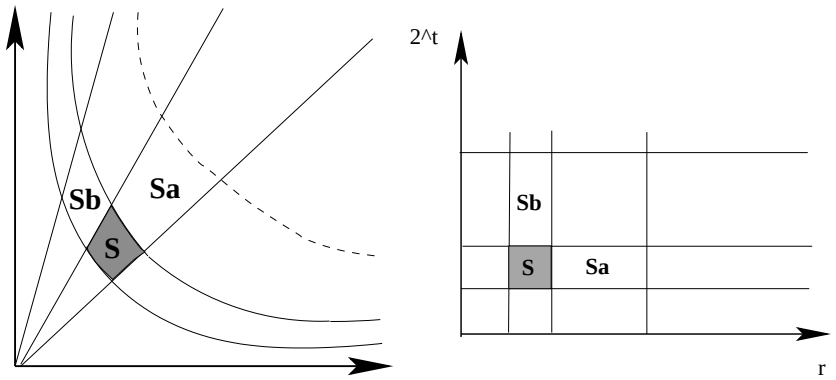

Fig. 4. *The figure on the left shows the hyperbolic trapezoid $S = S_I$, in quadrant I, and the action of the matrices a and b on it. The plot on the right shows the same regions in the coordinate system defined by r and 2^t.*

For any $k \neq 0$, the right action of B preserves the hyperbolas H_k since

$$\xi\, b_\ell = (\xi_1, \xi_2) \begin{pmatrix} (\sqrt{2})^{-\ell} & 0 \\ 0 & (\sqrt{2})^\ell \end{pmatrix} = (\xi_1(\sqrt{2})^{-\ell}, \xi_2(\sqrt{2})^\ell) = (\eta_1, \eta_2),$$

and $\eta_1\eta_2 = \xi_1\xi_2$. Hence, the right action of B maps an hyperbolic strip into itself. In addition, a direct calculation shows that, if $\xi_2 = m\xi_1$ and $(\eta_1, \eta_2) = (\xi_1, \xi_2)b_\ell$, then $\frac{\eta_2}{\eta_1} = 2^\ell \frac{\xi_2}{\xi_1} = 2^\ell m$. Hence, $b_\ell \in B$ maps a line through the origin

[2] The main ideas the hyperbolic construction were introduced by one of the authors and his collaborators in [26].

of slope m into a line through the origin of slope $2^\ell m$. From the observations above, it follows that the hyperbolic trapezoid

$$S_I = \{\xi(r,t) : 1 \le r < 2, 1 \le 2^t \le 2\}$$

is a tiling set of the hyperbolic strip $\{\xi(r,t) : 1 \le r < 2\}$ for the B dilations.

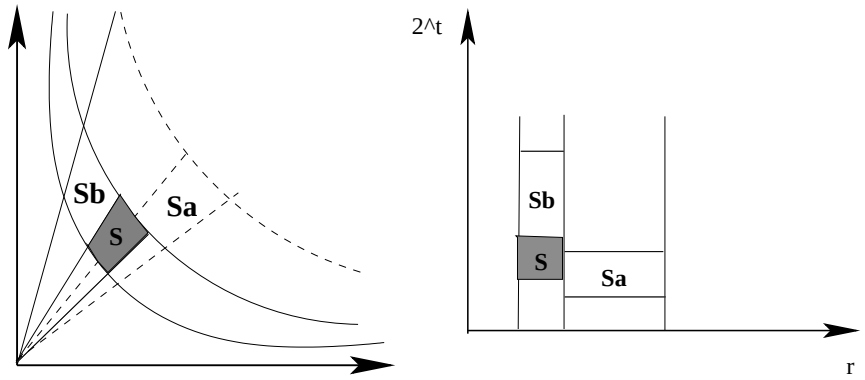

Fig. 5. *The plot on the left shows the hyperbolic trapezoid $S = S_I'$, in quadrant I, and the action of the matrices a and b on it. The plot on the right shows the same regions in the coordinate system defined by r and 2^t.*

Next let

$$A = \left\{ a^j = \begin{pmatrix} \sqrt{2} & 0 \\ 0 & \sqrt{2} \end{pmatrix}^j : j \in \mathbb{Z} \right\}. \tag{2}$$

Since a maps the hyperbola $\xi_1\xi_2 = k$ to the hyperbola $\xi_1\xi_2 = 2k$, it follows that a^j maps the hyperbolic strip $\{\xi(r,t) : 1 \le r < 2\}$ to the hyperbolic strip $\{\xi(r,t) : 2^j \le r < 2^{j+1}\}$. Figure 4 shows the hyperbolic trapezoid S_I and illustrates the action of a and b on S_I. The observations above imply that S_I is a tiling set of quadrant I for the A and B matrices, that is:

$$\bigcup_{j\in\mathbb{Z}} \bigcup_{\ell\in\mathbb{Z}} S_I a^j b^\ell = \text{quadrant I},$$

where the union is disjoint, up to sets of measure zero. To obtain a tiling of the whole frequency plane, let S_{III} be the symmetric extension of S_I in quadrant III, that is $S_{III} = \{x \in \mathbb{R}^2 : -x \in S\}$. Also, define another hyperbolic trapezoid in quadrant IV, namely

$$S_{IV} = \{(\xi_1, \xi_2) : (-\xi_1, \xi_2) \in S_I\}$$

and its symmetric extension S_{II} in quadrant II. It then follows that

$$\bigcup_{j\in\mathbb{Z}} \bigcup_{\ell\in\mathbb{Z}} (S_I \cup S_{II} \cup S_{III} \cup S_{IV})\, a^j b_\ell = \mathbb{R}^2,$$

where again the union is disjoint, up to sets of measure zero. Hence, letting $\Psi = (\psi_I, \psi_{II}, \psi_{III}, \psi_{IV})$, where $\hat{\psi}_I = \chi_{S_I}, \ldots, \hat{\psi}_{IV} = \chi_{S_{IV}}$, it follows from

Theorem 1 that the system of wavelets with composite dilations

$$\mathcal{A}_{AB}(\Psi) = \{D_a^j D_{b_\ell} T_k \Psi : j \in \mathbb{Z}, k \in \mathbb{Z}^2, \ell \in \mathbb{Z}\}$$

is a Parseval frame of $L^2(\mathbb{R}^2)$.

A variant of the construction above is obtained by replacing the set of diagonal matrices used above with the new set

$$A = \left\{ a^j = \begin{pmatrix} 2 & 0 \\ 0 & \sqrt{2} \end{pmatrix}^j : j \in \mathbb{Z} \right\}. \tag{3}$$

These matrices produce *parabolic scaling*, that it, the dilation factor along one orthogonal axis is quadratic with respect to the other axis. This scaling factor was found to be of fundamental importance in the construction of optimally sparse multiscale systems such as curvelets and shearlets [7,23,32].

Similarly to the construction above, let $\widetilde{S}_I$ be the hyperbolic trapezoid in the frequency plane defined by

$$\widetilde{S}_I = \{\xi(r,t) : \sqrt{2}/2 \leq r < 2, 1 \leq 2^t \leq 2\}.$$

Again, right action of B maps any hyperbolic strip into itself. The matrix $a \in A$ maps the hyperbola $\xi_1\xi_2 = k$ to the hyperbola $\xi_1\xi_2 = 2\sqrt{2}k$ and, thus, a^j maps the hyperbolic strip $\{\xi(r,t) : \sqrt{2}/2 \leq r < 2\}$ to the hyperbolic strip $\{\xi(r,t) : 2(2\sqrt{2})^{j-1} \leq r < 2(2\sqrt{2})^j\}$. Unlike the diagonal case, however, the matrix $a \in A$ does not preserve lines through the origin since it maps a line $\xi_2 = m\xi_1$ into $\xi_2' = \frac{\sqrt{2}}{2} m\xi_1'$. The action of the matrices a and b on $\widetilde{S}_I$ is shown in Figure 5, which also shows that the sets $S_I' a^i b_\ell$ become increasingly more elongated as $i \to \infty$. Similarly to the construction above, by defining trapezoids $\widetilde{S}_{II}, \widetilde{S}_{III}$ and $\widetilde{S}_{IV}$ in the other quadrants, it is easy to verify that also in this case we obtain a tiling of the frequency plane as:

$$\bigcup_{j\in\mathbb{Z}} \bigcup_{\ell\in\mathbb{Z}} (\widetilde{S}_I \cup \widetilde{S}_{II} \cup \widetilde{S}_{III} \cup \widetilde{S}_{IV})\, a^j b^\ell = \mathbb{R}^2.$$

Once more, let $\Psi = (\psi_I, \psi_{II}, \psi_{III}, \psi_{IV})$, where $\hat{\psi}_I = \chi_{\widetilde{S}_I}, \ldots, \hat{\psi}_{IV} = \chi_{\widetilde{S}_{IV}}$. It then follows from Theorem 1 that the system of wavelets with composite dilations

$$\mathcal{A}_{AB}(\Psi) = \{D_a^j D_{b_\ell} T_k \Psi : j \in \mathbb{Z}, k \in \mathbb{Z}^2, \ell \in \mathbb{Z}\}$$

is a Parseval frame of $L^2(\mathbb{R}^2)$.

2.2.1 Well-localized Construction

In order to construct hyperbolic systems of wavelets with composite dilations which are well-localized, it is useful to recall the following result.

Theorem 2 ([26]) *Let $\psi \in L^2(\mathbb{R}^2)$ be such that* $\operatorname{supp} \hat{\psi} \subset Q = [-1/2, 1/2]^2$, *and*

$$\sum_{j,\ell \in \mathbb{Z}} |\hat{\psi}(\xi\, a^j\, b^\ell)|^2 = 1 \quad \text{a.e. } \xi \in \widehat{\mathbb{R}}^2,$$

where $a, b \in GL_2(\mathbb{R})$. Then the system of wavelets with composite dilations (1)*, where $A = \{a^j : j \in \mathbb{Z}\}$ and $B = \{b^\ell : \ell \in \mathbb{Z}\}$, is a Parseval frame of $L^2(\mathbb{R}^2)$.*

For $\xi = (\xi_1, \xi_2) \in \widehat{\mathbb{R}}^2$, with $\xi_1 \neq 0$, let $\hat{\psi}$ be defined by

$$\hat{\psi}(\xi_1, \xi_2) = V(\xi_1 \xi_2)\, W(\frac{\xi_2}{\xi_1}), \tag{4}$$

where V, $W \in C_c^\infty(\mathbb{R})$ satisfy $\operatorname{supp} V \subset [\frac{1}{88}, \frac{1}{11}]$, $\operatorname{supp} W \subset [\frac{2}{3}, \frac{8}{3}]$,

$$\sum_{j \in \mathbb{Z}} |V(2^j r)|^2 = 1 \quad \text{for a.e. } r \geq 0,$$

and

$$\sum_{\ell \in \mathbb{Z}} |W(2^\ell 2^t)|^2 = 1 \quad \text{for a.e. } t \in \mathbb{R}.$$

The functions V and W can be obtained by appropriately rescaling a Meyer wavelet and restricting its domain to the positive axis in the Fourier domain.

Hence we have the following corollary of Theorem 2.

Proposition 1 *Let $\psi \in L^2(\mathbb{R}^2)$ be given by* (4) *and ψ' be defined by $\hat{\psi}'(\xi_1, \xi_2) = \hat{\psi}(-\xi_1, \xi_2)$. Then for A given by* (2) *and B given by* (1) *the system of wavelets with composite dilations*

$$\mathcal{A}_{AB}(\Psi) = \{D_a^j D_{b_\ell}\, T_k\, \Psi : j \in \mathbb{Z}, k \in \mathbb{Z}^2, \ell \in \mathbb{Z}\},$$

is a Parseval frame of $L^2(\mathbb{R}^2)$.

Proof. The support conditions on V, W ensure that $\operatorname{supp} \hat{\psi}$ is a pair of trapezoidal regions in quadrants I and III which are contained inside the unit cube $[-1/2, 1/2]^2$. In fact, V is constant along each branch of the hyperbola and is defined along lines through the origin. Its support is contained between the hyperbolas $\xi_1 \xi_2 = \frac{1}{88}$ and $\xi_1 \xi_2 = \frac{1}{11}$. W is constant along each line through the origin, is defined along hyperbolas and its support is contained in the cone defined by the lines through the origin of slopes $\xi_2 = \frac{2}{3}\, \xi_1$ and $\xi_2 = \frac{8}{3}\, \xi_1$.

In addition, a direct calculation shows that, for all $\xi = (\xi_1, \xi_2)$, with $\xi_1 \xi_2 \geq 0$ and $\xi_1 \neq 0$, we have:

$$\sum_{j \in \mathbb{Z}} \sum_{\ell \in \mathbb{Z}} |\hat{\psi}(\xi\, a^j\, b_\ell)|^2$$

$$= \sum_{j\in\mathbb{Z}} \sum_{\ell\in\mathbb{Z}} |\hat{V}(2^j\xi_1\xi_2)|^2 \, |W(2^\ell \frac{\xi_2}{\xi_1})|^2$$
$$= \sum_{j\in\mathbb{Z}} |\hat{V}(2^j\xi_1\xi_2)|^2 \sum_{\ell\in\mathbb{Z}} |W(2^\ell \frac{\xi_2}{\xi_1})|^2 = 1,$$

for ξ in quadrants I and III in $\mathbb{R}^2$. A similar calculation with $\hat{\psi}$ replaced by $\hat{\psi}'$ yields a similar result valid for all ξ in quadrants II and IV of $\mathbb{R}^2$. Hence $\sum_{j\in\mathbb{Z}} \sum_{\ell\in\mathbb{Z}} |\hat{\Psi}(\xi\, a^j\, b_\ell)|^2 = 1$, for a.e. $\xi \in \mathbb{R}^2$. The proof now follows from Theorem 2. $\square$

With a slight modification of the argument of Proposition 1 one can show that it is possible to construct a similar well-localized Parseval frame by replacing the set of isotropic dilations A given by (2) with the anisotropic dilations (3).

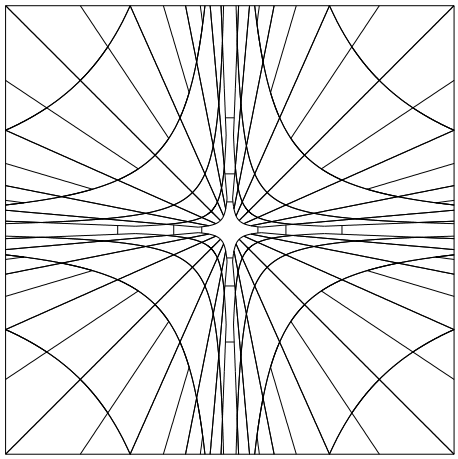

Fig. 6. *Tiling of the frequency domain associated with a hyperbolic system of wavelets with composite dilations.*

Notice that, for a discrete implementation of the hyperbolic systems described in this section, the indices j and ℓ need to be limited to a finite range. The asymptotic regions not covered because of this discretization can then be dealt with by partitioning the complementary regions with a Laplacian Pyramid-type of filtering. A form of the tiling of the frequency plane associated with this construction is illustrated in Figure 6. For the correct interpretations of this figure, it is important to observe that the elements of the well-localized system of wavelets with composite dilations $\psi(a^j b^\ell x)$ do overlap in the frequency domain. that is, Figure 6 should be interpreted as a picture of the essential frequency support (i.e., the regions where most of the norm is concentrated), rather than the exact frequency support of the elements of the system.

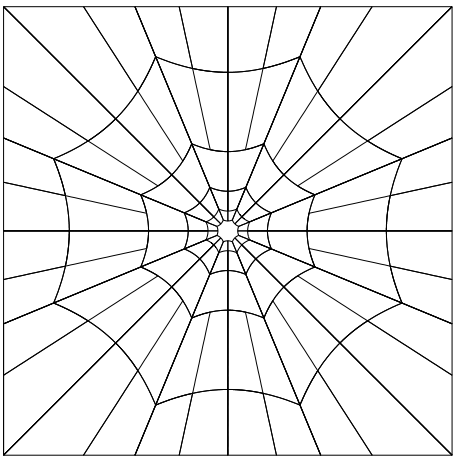

Fig. 7. *Frequency tiling of a cone-based hyperbolic composite wavelet system. Notice that the scaling matrix a is isotropic and the number of directional subbands is fixed at each scale. If the matrix a was replaced by an anisotropic one, e.g., the parabolic scaling matrix, then the number of directional subbands would double at each scale level.*

2.2.2 Cone-based hyperbolic construction

Like the case of shearlets, the hyperbolic construction suffers from a bias in directional sensitivity along the orientations $\pm\pi/4, \pm 3\pi/4$. In addition, the regions along the orthogonal axes in the frequency domain are only covered asymptotically, for values $\ell \to \pm\infty$. To overcome this situation, we define the "cone-based" system of wavelets of composite dilations

$$\{D_a^j \, D_{b_\ell} \, T_k, \psi : \, j \geq 0, |\ell| \leq L, k \in \mathbb{Z}^2\},$$

where $b_\ell \in B$ given by (1), a can be the isotropic or anisotropic dilation matrix, L is chosen so that the system tiles the frequency plane only in the cone $\frac{\pi}{8} \leq \frac{\xi_2}{\xi_1} \leq \frac{3\pi}{8}$, and ψ is given by (4). Using ψ' defined as in Proposition 1 one covers the frequency plane in the cone $\frac{5\pi}{8} \leq \frac{\xi_2}{\xi_1} \leq \frac{7\pi}{8}$. Finally, the remaining two cones in the frequency domain are covered by rotating the above systems by $\pi/4$. The picture of the frequency tiling associated with this decomposition is given in Figure 7.

3 Composite Wavelet Implementation

3.1 Analysis Filter Design

In this section, we describe a novel approach for the construction of filters that match the frequency tiling associated with the desired system of wavelets with composite dilations. That is, given a system of wavelets with composite

dilations $\mathcal{A}_{AB}(\Psi)$, this approach allows us to directly apply the set of matrices A and B to generate the specific spatial frequency tiling associated with the system $\mathcal{A}_{AB}(\Psi)$.

To describe our approach, consider a (generalized) wavelet $\hat{\psi}(\xi) = \chi_S(\xi)$, where S corresponds to a bounded region satisfying the conditions of Theorem 1. For example, S can be chosen to be a trapezoidal hyperbola and the set of matrices A and B to be $A = \{a^j\}$, $B = \{b_\ell\}$, as in Construction 4.

Hence, given a sequence of points $\{(\xi_1^n, \xi_2^n)\}_{n=1}^N \in S$ that densely fills the set S, we define $(\overline{\xi}_1^n, \overline{\xi}_2^n) = \lceil (\xi_1^n, \xi_2^n) \rceil = (\lceil \xi_1^n \rceil, \lceil \xi_2^n \rceil)$, where $\lceil \cdot \rceil$ denotes the ceiling function. To digitally create the desired filters, we assign the non-zero entries of our starting filter $\widehat{G}_{0,0}$ by the evaluation $\widehat{G}_{0,0}(\overline{\xi}_1^n, \overline{\xi}_2^n) = 1$. We then proceed to create the other filters $\{\widehat{G}_{i,\ell}\}$ by assigning the non-zeros entries as $\widehat{G}_{i,\ell}(\overline{\eta}_1^n, \overline{\eta}_2^n) = 1$ for $(\overline{\eta}_1^n, \overline{\eta}_2^n) = \lceil (\xi_1^n, \xi_2^n)\, a^j b_\ell \rceil$. Note that N needs to be chosen large enough so that the points $(\overline{\eta}_1^n, \overline{\eta}_2^n)$ are dense enough to fill out the regions $S_{j,\ell} = S a^j b_\ell$ completely in terms of its pixelated image for all desired values of j and ℓ. Figure 8 illustrates this construction.

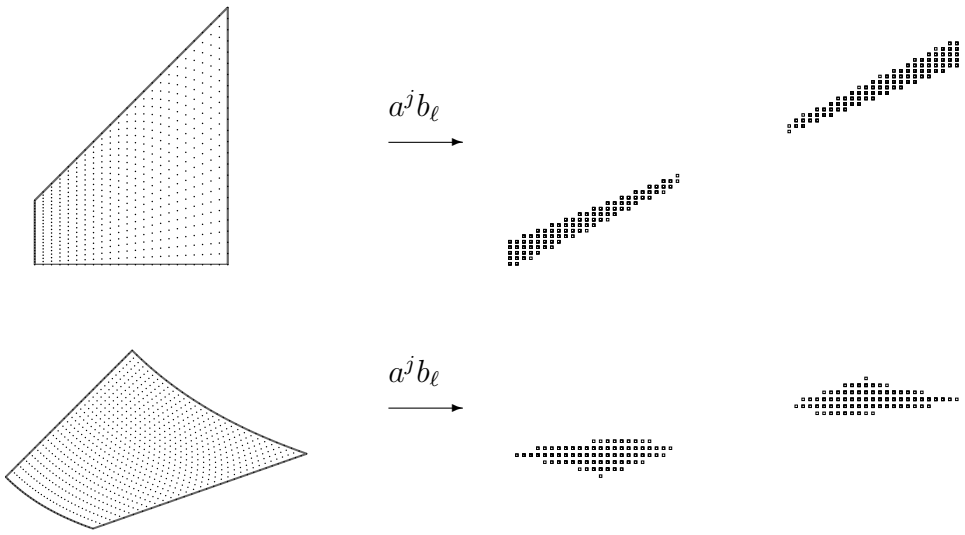

Fig. 8. Illustrations of filter constructions where the number of samples used is small for the purpose of presentation. The images on the left are the sequences of points $\{(\xi_1^n, \xi_2^n)\}_{n=1}^N$ contained in the region S. The images on the right are the sequences of points $\{(\overline{\eta}_1^n, \overline{\eta}_2^n)\}_{n=1}^N$ where $(\overline{\eta}_1^n, \overline{\eta}_2^n) = \lceil (\xi_1^n, \xi_2^n) a^j b_\ell \rceil$.

This construction can be modified to create the well-localized version of wavelets of composite dilations by the following modification. We start by creating an initial densely supported filter with the desired windowing. By keeping track of the multiple assigned grid points, the windowing can be appropriately com-

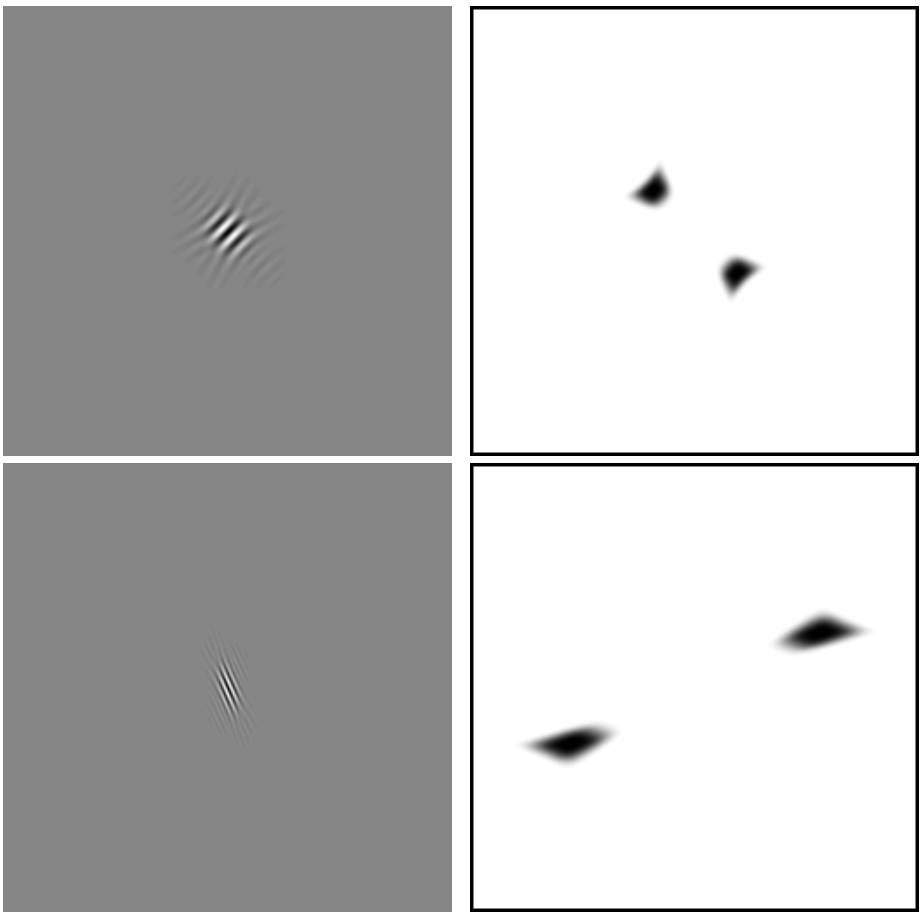

Fig. 9. *Examples of hyperbolic filters. From left to right: Time Domain, Frequency Domain*

pensated by assigning the average windowed value at these point locations. Examples of this construction are shown in Figure 9 and a pseudo-code for creating such filters is given in the Appendix.

This construction process can be applied to any generic planar region and can be viewed as a refinement of the original discrete shearlet transform construction given in [16]. In fact, when the techniques suggested in this paper are used to design filters for a revised discrete shearlet transform, the newly constructed discrete transform performs significantly better than its first incarnation. Recall that the original shearlet implementation was based on the use of a mapping function that performed a re-arrangement of windowed data in a pseudo-polar grid onto a Cartesian grid. In our new implementation, we avoid the use of the mapping function and are able to produce the appropriate windowed data directly onto the Cartesian grid. In addition, this implementation is multi-channel, so that the estimates provided from individual filtered coefficients are not level-dependent and this improves the transform's conditioning. See Figure 10 for a representative illustration of the filters associated with the new implementation.

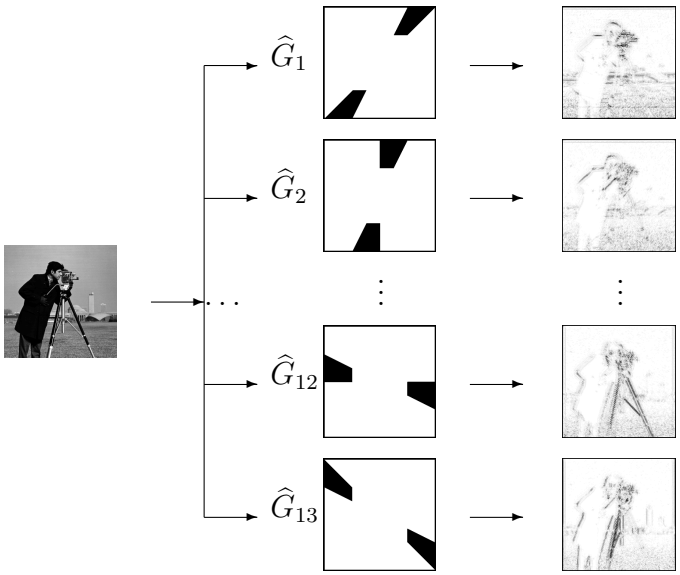

Fig. 10. An illustration of a multi-channel filter bank designed to implement wavelets with composite dilations such as the shearlet transform.

Also notice that, in the approach from [16], it was the inverse mapping function that took care of weighting the multiple assigned pixel values. By avoiding the re-mapping process, we can now avoid creating re-arrangement domains (a process which usually generated some artefacts). In fact, we are able to obtain the desired filters directly by applying the sets of A and B matrices associated with the desired composite wavelet decompositions. This way, the discrete implementation provides a perfect match with its theoretical counterpart and it allows one to deal even with wavelets with composite dilations associated with very complicated geometrical decompositions in the spatial frequency plane.

3.2 Synthesis Filter Design

It would seem that our construction method of analysis filters should be extendable for the creation of the synthesis filters. However, by dealing with the non-uniformity caused by the discretization of a continuous formulation, we have introduced slight imperfections in the windowing. These slight deviations can be particularly unforgiving in a multi-channel based implementation. Consider, as an example, reformulating the contourlet transform naively into a multi-channel implementation by applying the transform to a delta function to find the analysis and synthesis filters. Figure 11 gives a visual illustration of how this approach fails to achieve perfect reconstruction. This is particularly interesting since the standard implementation of contourlets achieves perfect reconstruction.

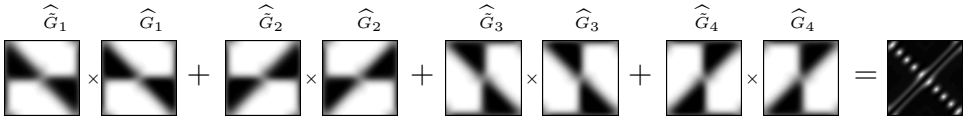

Fig. 11. By applying the nonsubsampled contourlet transform to a delta function, we can obtain directional filters. Failure of the perfect reconstruction condition is depicted using the analysis and synthesis filters found by applying the 2nd level decomposition of contourlets to a delta function.

To improve upon the reconstruction estimate, we will construct the synthesis filters by using a method devised for solving a related problem known as the Multichannel Deconvolution Problem (MDP) which can roughly be stated as follows. *Given a collection* $\{G_i\}_{i=1}^m$ *of distributions on* $\mathbb{R}^d$ *(*$d \geq 2$*), find a collection* $\{\tilde{G}_j\}_{j=1}^m$ *of distributions such that*

$$\sum_{j=1}^{m} \tilde{G}_j * G_j = \delta,$$

where δ *is a Dirac delta distribution.* In the Fourier-Laplace domain, when the distributions are assumed to be compactly supported, this equation is referred to as the *analytic Bezout equation*. This problem has a connection with the polynomial Bezout equation which is usually solved for computing the filters associated with traditional filter banks (see [10] for more details).

Several methods for solving the MDP in a discrete setting provide a way of constructing appropriate synthesis filters (see [37,38,2,3,28,17,10,46] for details on some of these methods). One of the earliest and simplest methods for solving this problem was given in [37]. To explain its derivation, we formulate the problem in the Fourier domain as follows. Suppose we wish to recover the image f and that we are given m blurred images s_j, i.e.

$$\widehat{s_j}(\xi_1, \xi_2) = \widehat{f}(\xi_1, \xi_2)\, \widehat{G_j}(\xi_1, \xi_2) + \widehat{n_j} \text{ for } j = 1, \ldots, m,$$

where G_j and n_j are the respective transfer function and associated noise from the j-th imaging sensor. Assuming that no statistical information is available, find the image f_a which yields a least squares fit between predicted and observed images, i.e., minimize

$$\sum_{j=1}^{m} |\widehat{s_j}(\xi_1, \xi_2) - \widehat{f_a}(\xi_1, \xi_2)\, \widehat{G_j}(\xi_1, \xi_2)|^2.$$

After differentiating with respect to $\overline{\widehat{f_a}}$, the solution is found to be

$$\widehat{f_a}(\xi_1, \xi_2) = \sum_{j=1}^{m} \widehat{s_j}(\xi_1, \xi_2)\, \widehat{\tilde{G}_j}(\xi_1, \xi_2),$$

where

$$\widehat{\tilde{G}_j}(\xi_1,\xi_2) = \frac{\overline{\widehat{G_j}}(\xi_1,\xi_2)}{\sum_{k=1}^{m} |\widehat{G_k}(\xi_1,\xi_2)|^2},$$

for $j = 1, \ldots, m$.

The synthesis filters $\{\tilde{G}_j\}_{j=1}^m$ are robust (and even optimal) with respect to any residual noise left from the decompositions that might remain after thresholding schemes have been utilized for denoising purposes. When filters of small finite support are desired, we use the method given in [10], which reduces the problem of finding the synthesis filters to solving a constrained matrix inversion problem. This method is particularly flexible as the support sizes of the synthesis filters can be controlled by a free parameter that balances between local and global conditioning.

Another solution to achieve perfect recontruction is to slightly modify the analysis filters to be

$$\widehat{G_j}(\xi_1,\xi_2) = \frac{\widehat{G_j}(\xi_1,\xi_2)}{\sqrt{\sum_{k=1}^{m} |\widehat{G_k}(\xi_1,\xi_2)|^2}}, \tag{5}$$

and to use

$$\widehat{\tilde{G}_j}(\xi_1,\xi_2) = \frac{\overline{\widehat{G_j}}(\xi_1,\xi_2)}{\sqrt{\sum_{k=1}^{m} |\widehat{G_k}(\xi_1,\xi_2)|^2}}, \tag{6}$$

as the synthesis filters for $j = 0, \ldots, m-1$. Note that this solution means that the implemented transform corresponds to a tight frame. However, we have found that for some constructions the MDP solutions perform better.

To emphasize the benefits of our proposed filter constructions, we show the differences in frequency responses for some representatives of the new shearlet filters and the non-subsampled contourlet transform (NSCT) filters in Figure 12. This illustration shows that whereas the NSCT filters may be constructed by using conventional filter design elements, their desired frequency responses do not truly match with the actual frequency responses. Nonetheless, the NSCT filters are very effective and have other advantages.

Hence, using the notation introduced above, we summarized the algorithm for the construction of the filters implementing the discrete wavelets with composite dilations as follows:

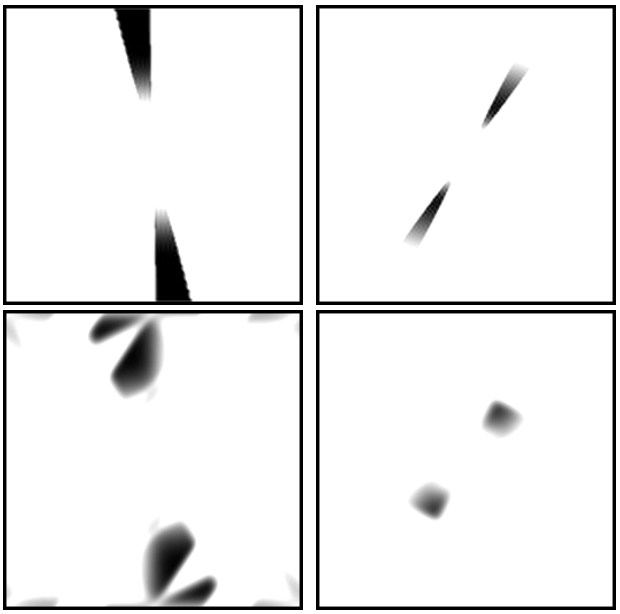

Fig. 12. Comparison of filters design methods. The images on the top correspond to examples of the frequency responses of the newly constructed shearlet filters. The images on the bottom correspond to examples of the frequency responses of the NSCT for the same directional components.

(1) Generate a sequence of points $\{(\xi_1^n, \xi_2^n)\}_{n=1}^N \in S$ filling densely the support region S associated with the generator of the system of wavelets with composite dilations.
(2) Given j and ℓ, form filter $\widehat{G}_{j,\ell}$ by assigning the value at $(\overline{\eta}_1^n, \overline{\eta}_2^n) = \lceil (\xi_1^n, \xi_2^n) a^j b_\ell \rceil$ to be the average of the pre-image values of the generator function evaluated at (ξ_1^n, ξ_2^n).
(3) Use synthesis filters $\widehat{\widetilde{G}}_{j,\ell}(\xi_1, \xi_2) = \dfrac{\overline{\widehat{G}}_{j,\ell}(\xi_1, \xi_2)}{\sum_{j,\ell} |\widehat{G}_{j,\ell}(\xi_1, \xi_2)|^2}$, solve for synthesis filters by solving the matrix system as described in [10], or use (5) and (6).

Note that the filterbank implementation is highly efficient as it requires $O(N^2 \log N)$ operations for an $N \times N$ image.

4 Numerical Experiments

In this section, we present several numerical experiments on image restoration and enhancement to demonstrate the effectiveness of the wavelets with composite dilations and their discrete implementation.

4.1 Denoising

In the first set of experiments, we illustrate the denoising capability of the new wavelets with composite dilations by means of hard thresholding.

The objective of this problem is to recover an image x, given noisy observations

$$y = x + \gamma,$$

where γ is zero-mean white Gaussian noise with variance σ^2. By adapting the standard wavelet shrinkage approach [35], we apply a hard threshold on the subband coefficients of several versions of composite wavelets decompositions. In particular, we choose the threshold $T_j = K\sigma_j$, where σ_j^2 is the noise variance in each subband and K is a constant. In our experiments, we set $K = 2$ for all subbands.

To assess the denoising performance of our method, we compare it against three different competing discrete multiscale transforms: the nonsubsampled wavelet transform (NSWT), the curvelet transform (curv), and the nonsubsampled contourlet transform (NSCT). The discrete wavelets with composite dilations we have tested are the new shearlet transform (*ab-shear*), the cone-based hyperbolic transform (*c-hyper*), the hyperbolic transform (*hyper*), the star-like transform given in Construction 1 (*ab-star*). For the sake of comparison, we have also included the original implementation of the shearlet transform (*shear*) [16]. The peak signal-to-noise ratio (PSNR) is used to measure the performance of the different transforms. Recall that, given an $N \times N$ image x and its estimate $\tilde{x}$, the PSNR in decibels (dB) is defined as

$$PSNR = 20 \log_{10} \frac{255N}{\|x - \tilde{x}\|_F},$$

where $\|.\|_F$ is the Frobenius norm. In Tables I and II, we show the results obtained using various discrete transforms on the *Peppers* and *Barbara* images, respectively. The highest PSNR for each experiment is shown in bold. As it can be seen from the tables, all our new transforms provide superior or comparable results to that obtained using NSWT, NSCT and curvelets. Indeed, in some cases, the composite wavelet transforms provide improvement of nearly 1 dB or more compared to the competing algorithms. Figures 13, 14, 15 and 16 show some of the reconstructed images for these various experiments.

4.2 Enhancement

The objective of image enhancement is to improve the visual or perceptual quality of an image in a certain sense. For example, a simple and well-known

Fig. 13. Denoising experiments with a *Barbara* image. (a) Original image. (b) Noisy image with $\sigma = 20$, PSNR=22.15 dB. (c) Restored image using ab-shear, PSNR=30.38 dB . (d) Restored image using c-hyper, PSNR=30.41 dB. (e) Restored image using hyper, PSNR=30.49 dB. (f) Restored image using ab-star, PSNR=29.02 dB.

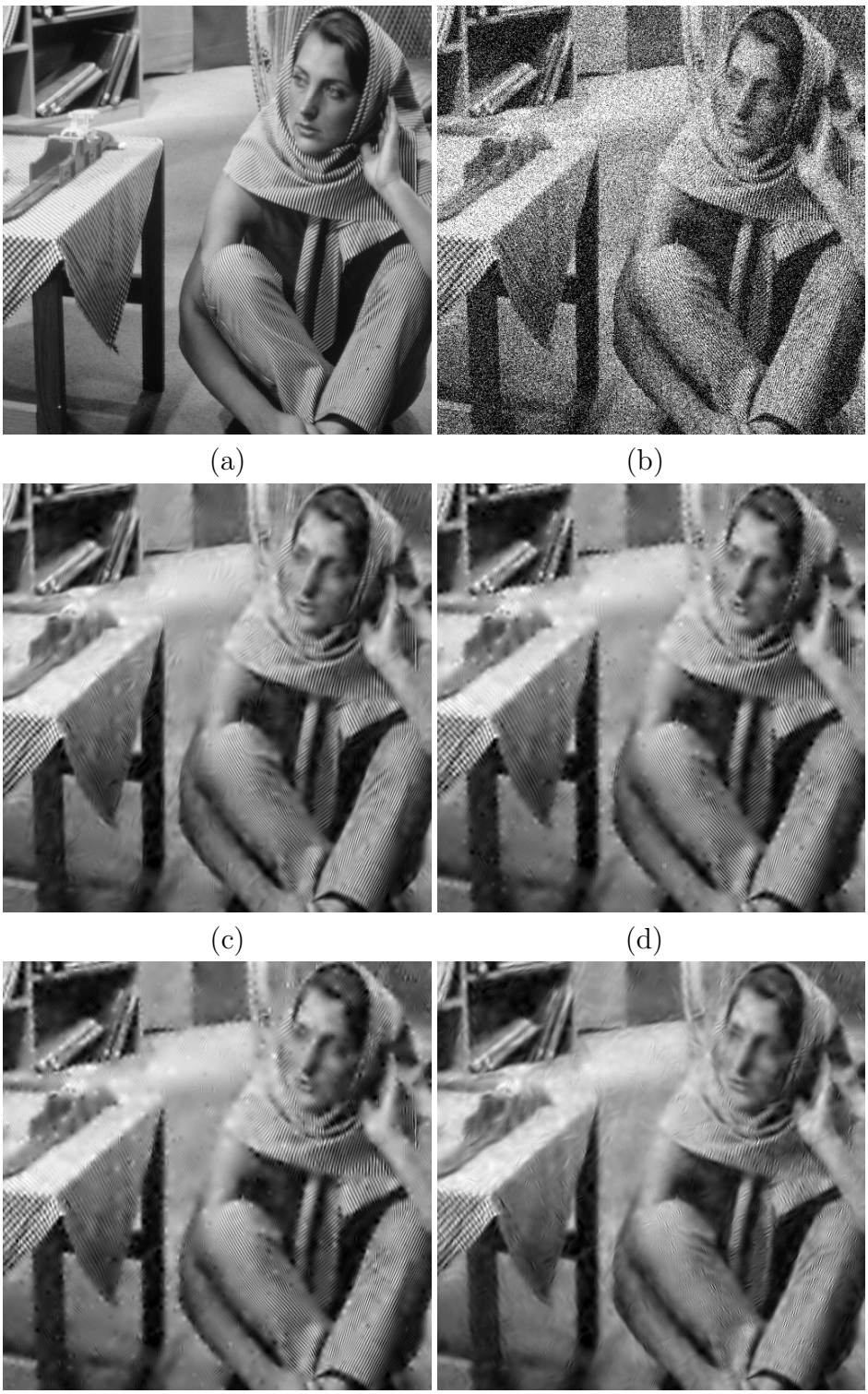

Fig. 14. Denoising experiments with a *Barbara* image. (a) Original image. (b) Noisy image with $\sigma = 50$, PSNR=14.20 dB. (c) Restored image using ab-shear, PSNR=25.59 dB . (d) Restored image using c-hyper, PSNR=25.78 dB. (e) Restored image using hyper, PSNR=25.35 dB. (f) Restored image using ab-star, PSNR=24.06 dB.

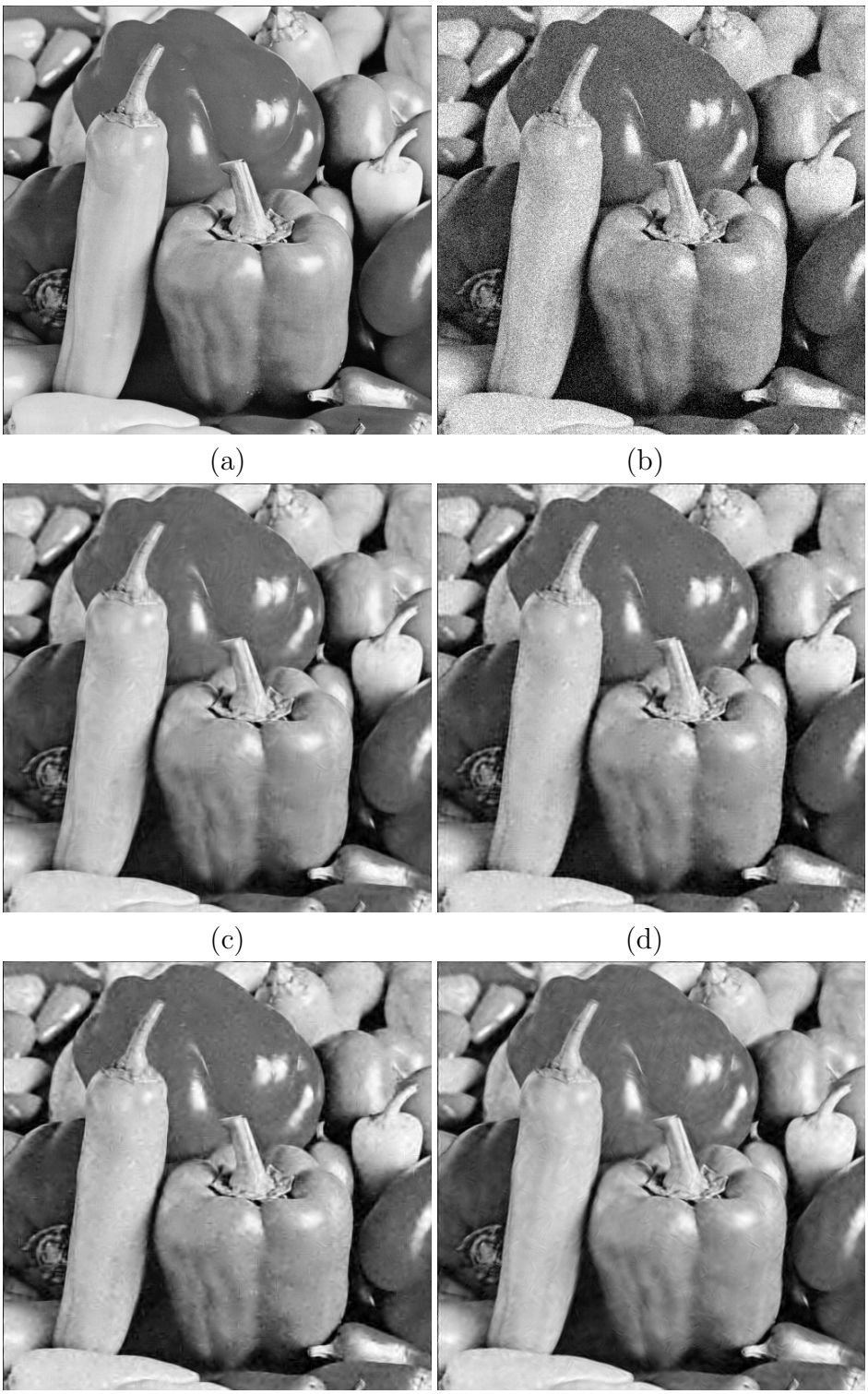

Fig. 15. Denoising experiments with a *Peppers* image. (a) Original image. (b) Noisy image with $\sigma = 20$, PSNR=22.15 dB. (c) Restored image using ab-shear, PSNR=31.82 dB . (d) Restored image using c-hyper, PSNR=31.01 dB. (e) Restored image using hyper, PSNR=31.28 dB. (f) Restored image using ab-star, PSNR=30.83 dB.

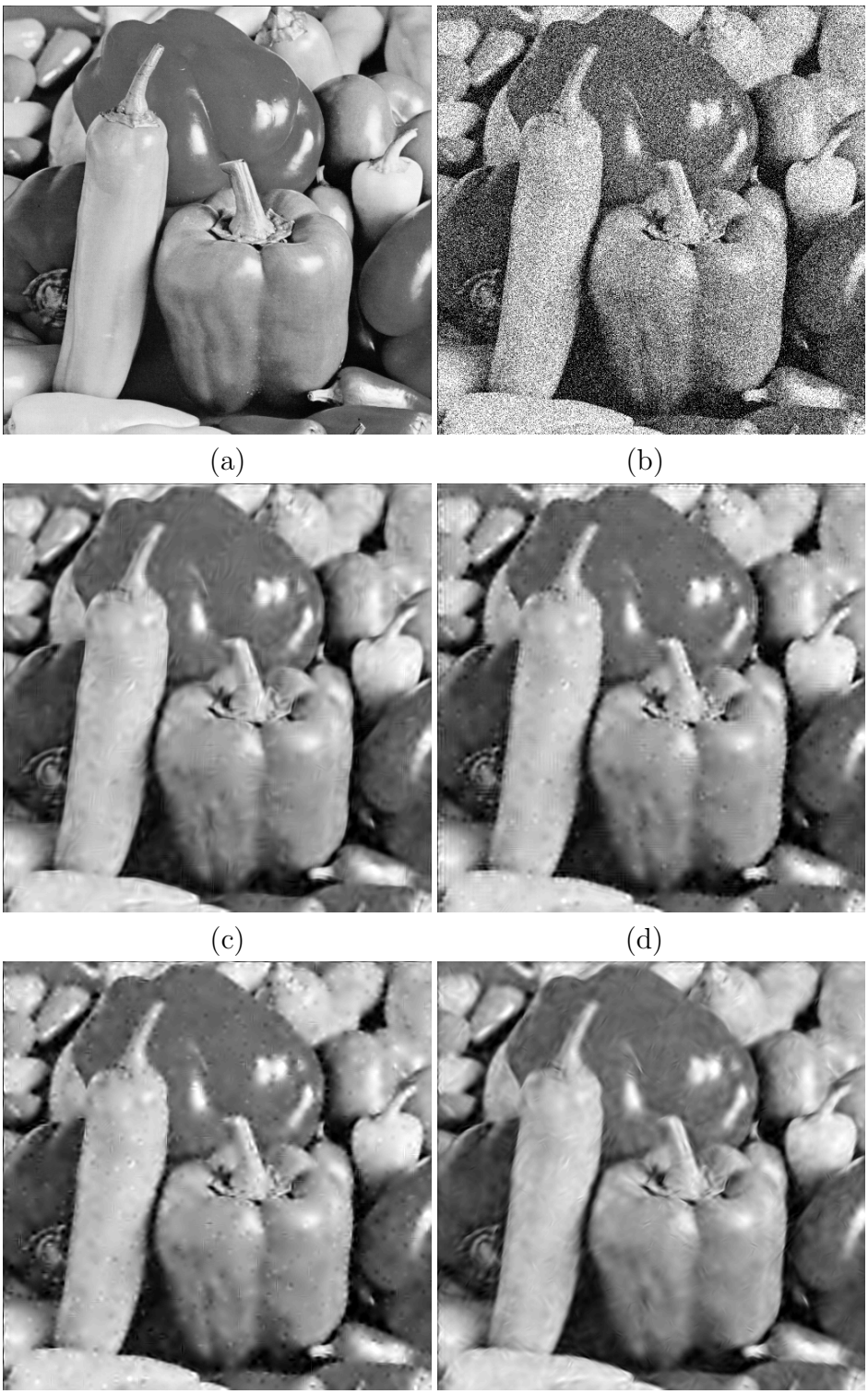

Fig. 16. Denoising experiments with a *Peppers* image. (a) Original image. (b) Noisy image with $\sigma = 50$, PSNR=14.20 dB. (c) Restored image using ab-shear, PSNR=27.98 dB . (d) Restored image using c-hyper, PSNR=27.17 dB. (e) Restored image using hyper, PSNR=27.33 dB. (f) Restored image using ab-star, PSNR=26.99 dB.

Table I: Denoising results using *Peppers* image.

σ	Noisy	ab-shear	c-hyper	hyper	ab-star	NSWT	shear	NSCT	curv
10	28.17	**34.28**	33.70	33.91	33.45	33.71	34.05	33.81	32.36
20	22.15	**31.82**	31.01	31.28	30.83	31.19	31.78	31.60	29.65
30	18.63	**30.25**	29.35	29.72	29.26	29.43	30.13	30.07	28.25
40	16.13	**29.01**	28.12	28.40	28.04	28.09	28.86	28.85	27.28
50	14.20	**27.98**	27.17	27.33	26.99	27.04	27.90	27.82	26.46

Table II: Denoising results using *Barbara* image.

σ	Noisy	ab-shear	c-hyper	hyper	ab-star	NSWT	shear	NSCT	curv
10	28.17	33.47	**33.97**	33.81	32.29	31.58	33.12	33.01	29.16
20	22.15	30.38	30.41	**30.49**	29.02	27.23	30.07	29.41	25.46
30	18.63	28.44	28.37	**28.53**	27.02	25.10	28.16	27.24	24.42
40	16.14	**26.93**	26.86	26.75	25.55	24.02	26.59	25.79	23.81
50	14.20	25.59	**25.78**	25.35	24.06	23.37	25.39	24.79	23.33

method to visually improve images with poor intensity is contrast enhancement using histogram equalization.

Since edges frequently contain the dominant information of an image, an effective way to improve the contrast of the image consists in enhancing the edges. This approach has been widely used in astronomical and medical imaging and many of the methods employed to this task are based on multiscale image decomposition. However, in most of these methods, the image is decomposed in a separable fashion, without taking full advantage of the geometric information associated with the edges [34,29]. By contrast, a multiscale decomposition which is able to take advantage of directional features, such as curvelets, shearlets or wavelets with composite dilations, is much more effective in dealing with the edges and other directional information [15,45,41,11]. At the same time, it is well-known that natural images have their energy strongly concentrated at low frequencies. Since directional information is related mostly to mid- and high-frequency components, the lowpass information can hinder our ability to efficiently capture and analyze these features. Therefore, scale information needs to be used in conjunction with directional information in applications where it is important to distinguish features of different sizes. To this end, in this section, we exploit the directional and multiscale properties of the newly designed wavelets with composite dilations for a new algorithm for image enhancement.

Our approach is based on the usage of a nonlinear mapping function which amplifies weak edges and suppresses noise. Specifically, we introduce a new adaptive nonlinear mapping function that incorporates the nonnegative garrote shrinkage functions. This approach provides a good compromise between hard and soft shrinkage rules and allows one to avoid amplifying noise and remove small noise perturbations. This nonlinear mapping f is defined as

$$f(y) = \begin{cases} 0 & \text{if } |y| < T_1, \\ \text{sign}(y)T_2 + \bar{\alpha}(\text{sigm}(c(g_y - \beta)) - \text{sigm}(-c(g_y + \beta))) & \text{if } T_2 \leq |y| \leq T_3, \\ y & \text{otherwise.} \end{cases}$$

where $\text{sigm}(y) = (1 + e^{-y})^{-1}$, $y \in [-1, 1]$, $\bar{\alpha} = \alpha(T_3 - T_2)$, $\beta \in (0, 1)$, c is a gain factor, $0 \leq T_1 \leq T_2 < T_3 \leq 1$, and $g_y = \frac{\text{garrote}_{T_2}(y)}{T_3 - T_2}$, with

$$\text{garrote}_{T_2}(y) = \begin{cases} 0, & \text{for } |y| \leq T_2 \\ y - \frac{T_2^2}{y}, & \text{for } |y| > T_2 \end{cases}$$

Notice that α can be computed by $\alpha = (\text{sigm}(c(1-\beta)) - \text{sigm}(-c(1+\beta)))^{-1}$. Here, β and c determine the threshold and the rate of enhancement, respectively. As can be seen from Figure 17, when the mapping f is applied to the composite wavelet transform of an image, only the values falling in the interval $[T_2, T_3]$ are modified for enhancement, while the values in $[0, T_1]$ are suppressed. These parameters can be adaptively estimated by using the robust median operator [8] and the noise variance in each subband of the image decomposition [42]. For example, T_1, T_2, and T_3 for the subband j can be chosen as $p\sigma_j, q\sigma_j, r\sigma_j$, respectively, where σ^2 is the noise variance of the input image and σ_j^2 is the noise variance of the jth subband and p, q and r are user defined values. Through this nonlinear function, the values of the transformed image in each subband can be pointwise modified for image enhancement by

$$\tilde{y_k} = y_{k_{\max}} f\left(\frac{y_k}{y_{k_{\max}}}\right),$$

where $1 \leq k \leq m$, y_k is the output of the kth channel of the filter bank, and $y_{k_{\max}}$ is the maximum absolute amplitude of y_k.

To summarize, our method for image enhancement using the discrete wavelet transform with composite dilations consists of the following steps:

(1) Estimate the noise standard deviation in the $N \times N$ input image using the robust median operator [8].
(2) Pass the input image through the analysis part of the filter bank. At this point, we get a set of m subbands, each corresponding to a given scale and direction. Each subband contains N^2 coefficients.

(3) For each subband:
   (a) Calculate the noise standard deviation [41].
   (b) Use the nonlinear mapping function to modify the subband coefficients.

(4) Pass the modified coefficients through the synthesis part of the filter bank and reconstruct the enhanced image.

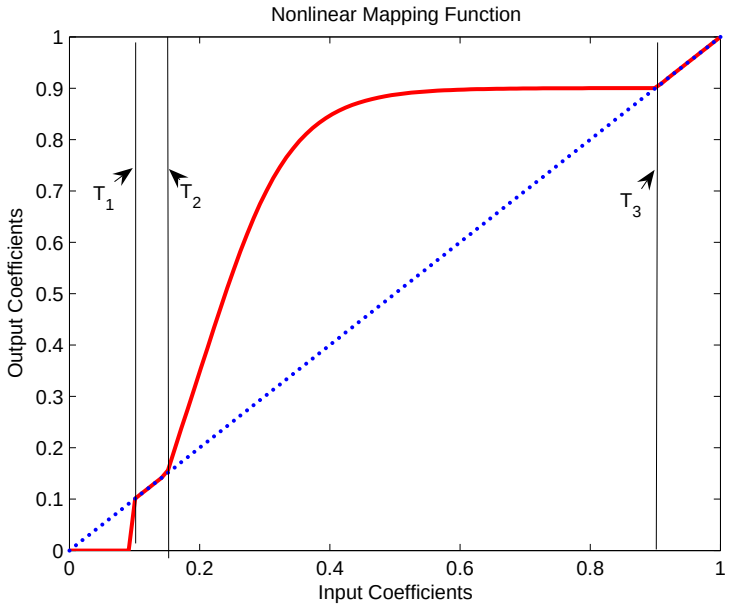

Fig. 17. Enhancement map: $\beta = 0.20, c = 25, T_1 = 0.1, T_2 = 0.15, T_3 = 0.9$.

Even though there is no standard way of evaluating the quality of enhanced images, a number of metrics have been proposed to quantitative analyze the enhanced images. One such metric is the Universal Quality Index (UQI) [44]. UQI models image distortion as a combination of three factors: loss of correlation, luminance distortion and contrast distortion. UQI takes values between -1 and 1, with 1 providing the best estimate of quality. We use this metric to evaluate the performance of our image enhancement algorithm on different tilings.

We have compared our method against the NSWT, NSCT and curv. The same nonlinear map is used for all our tests. In the first set of experiments, we used the classical *Barbara* image and the following parameters $\beta = 0.22$ and $c = 15$. Figures 18(b)-(f) and Figures 19(a)-(b) indicate that our proposed enhancement algorithm works better using the wavelets with composite dilations developed in this paper than using the NSWT and curv. The ab-shearlet tiling-based enhancement gives results visually similar to that of NSCT.

In the second set of experiments, the input image is a *Zebra* image, as shown in Figure 20(a). For this set of experiments, we chose $\beta = 0.20$ and $c = 0.15$ for this set of experiments. Figures 20(b)-(f) and Figures 21(a)-(b), show the

Fig. 18. Enhancement experiments with a *Barbara* image. (a) Original image. (b) Enhanced using NSWT. (c) Enhanced using ab-shear. (d) Enhanced using hyper. (e) Enhanced using c-hyper. (f) Enhanced using ab-star.

(a) (b)

Fig. 19. Enhancement experiments with a *Barbara* image. (a) Enhanced using NSCT. (b) Enhanced using curv.

results obtained by various transforms. As we see consistently from all these figures, the enhancement algorithm based on wavelets with composite dilations is very effective in enhancing the weak edges and retaining textures while suppressing the noise. This can be confirmed by looking at the UQI metrics in Table III.

Table III: UQI results for image enhancement experiments.

Image	ab-shear	c-hyper	hyper	ab-star	NSWT	NSCT	curv
Barbara	0.6918	**0.7027**	0.6953	0.6672	0.6750	0.6923	0.6687
Zebra	0.6538	0.6853	**0.6873**	0.6827	0.6800	0.6827	0.6820

4.3 Deconvolution Example

When the model of the degradation of an image is described as a convolution operation, the processing of recovering the original image from the degraded blurred image is commonly referred to as *deconvolution*. This inverse processes is known to be an ill-posed problem.

In this subsection, we give some preliminary experiments that indicate the ability of using a hyperbolic composite wavelet to better regularize the deconvolution process. The key point to make is that regularization for this type of problem is best done by using a representation that can sparsely represent the image and the convolution operator.

Let γ denote an $N \times N$ array of samples from a zero mean additive white Gaussian noise (AWGN) with variance σ^2. In addition, we let the $N \times N$ arrays y and x denote the observed image and the image to be estimated,

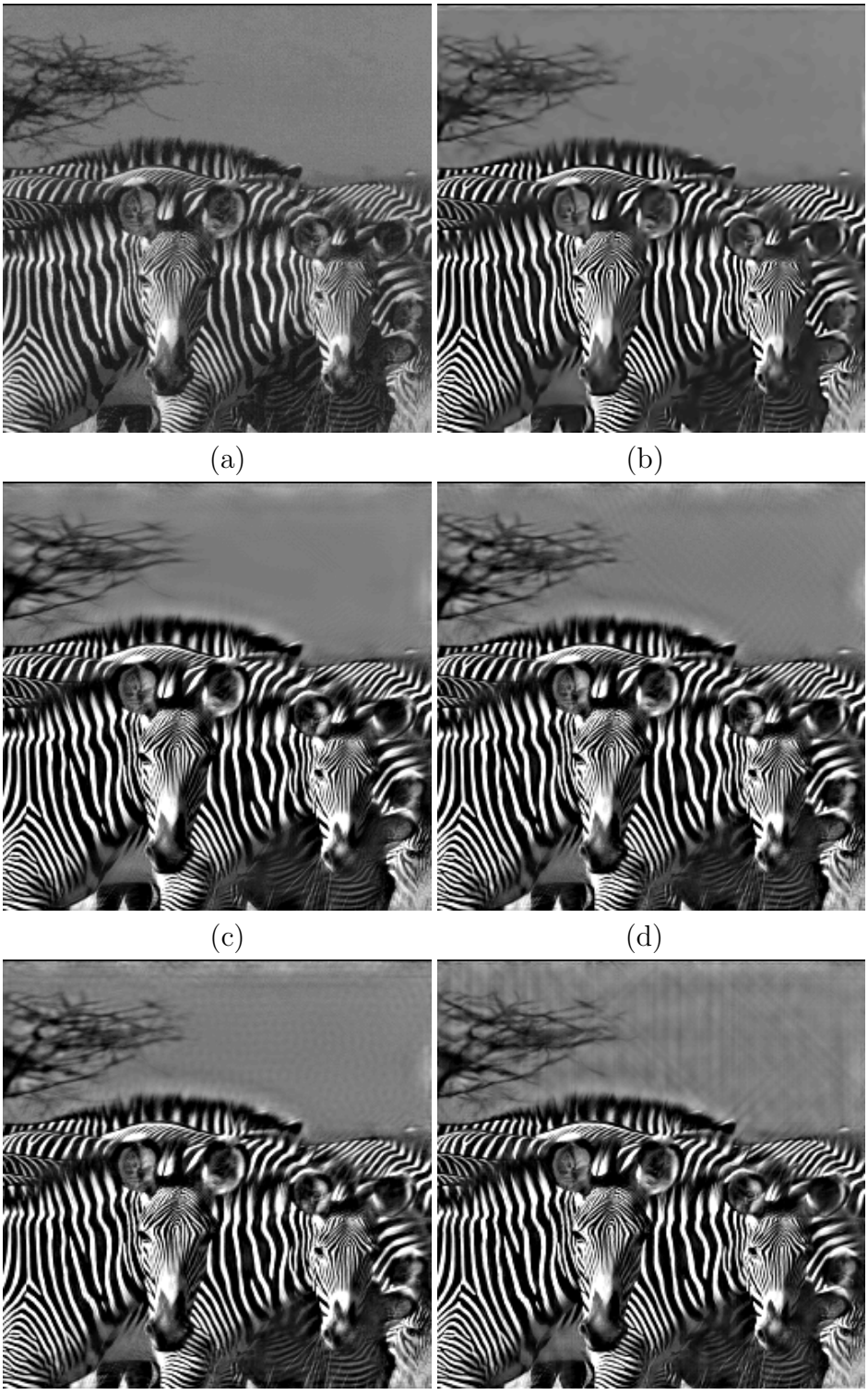

Fig. 20. Enhancement experiments with a *Zebra* image. (a) Original image. (b) Enhanced using NSWT. (c) Enhanced using ab-shear. (d) Enhanced using hyper. (e) Enhanced using c-hyper. (f) Enhanced using ab-star.

(a) (b)

Fig. 21. Enhancement experiments with a *Zebra* image. (a) Enhanced using NSCT. (b) Enhanced using curv.

respectively. When the blurring function is symmetric about the origin and a reflexive boundary is assumed for the finite discretization of the problem, the convolution is diagonalizable in a DCT domain. Thus we can write the deconvolution problem in the DCT domain as

$$Y(k_1, k_2) = \mathcal{H}(k_1, k_2)X(k_1, k_2) + \Gamma(k_1, k_2), \tag{7}$$

where $Y(k_1, k_2), \mathcal{H}(k_1, k_2), X(k_1, k_2)$ and $\Gamma(k_1, k_2)$ are the 2D DCTs of y, h, x, and γ, respectively, for $1 \leq k_1, k_2 \leq N$.

Figure 22 displays a contour plot of a typical out-of-focus blur in the DCT domain. Figure 22 also shows the corresponding hyperbolic composite decomposition when we consider the transform that results when the convolution is implemented with a reflexive boundary.

Using the regularized inverse operator $H_\alpha(k_1, k_2) = \mathcal{H}(k_1, k_2)/(\mathcal{H}(k_1, k_2)^2 + \alpha)$ for some regularizing parameter $\alpha \in R^+$, an image estimate in the DCT domain is given by

$$X_\alpha(k_1, k_2) = Y(k_1, k_2)H_\alpha(k_1, k_2),$$

for $1 \leq k_1, k_2 \leq N$. This type of regularization applied is often referred to as *Tikhonov-regularization*. Let $G_{j,\ell}$ denote the DCT of the composite wavelet filters $g_{j,\ell}$ for a given choice of j and ℓ. The coefficients of an estimate of the image for a given regularization parameter $\alpha_{j,\ell}$ can be computed in the DCT domain as

$$X_{\alpha_{j,\ell}}(k_1, k_2) = Y(k_1, k_2)G_{j,\ell}(k_1, k_2)H_{\alpha_{j,\ell}}(k_1, k_2)$$

for $1 \leq k_1, k_2 \leq N$. Taking advantage of the hyperbolic-based decomposition, we can adaptively control the regularization parameter to be the best suited

for each hyperbolic supported region. The final estimate is then found by inverting the composite wavelet transform using these estimated coefficients.

We compared this method against the standard Tikhonov-regularization using the *Barbara* image and out-of-focus point spread function shown in Figure 22. The results are provided in Table IV for various levels of noise given in terms of the BSNR. For an image of size $N \times N$, the BSNR is defined in decibels as

$$BSNR = 10 \log_{10} \left(\frac{\|(x * h) - \mu(x * h)\|_2^2}{N^2 \sigma^2} \right),$$

where $\mu(x * h)$ denotes the mean of $x * h$.

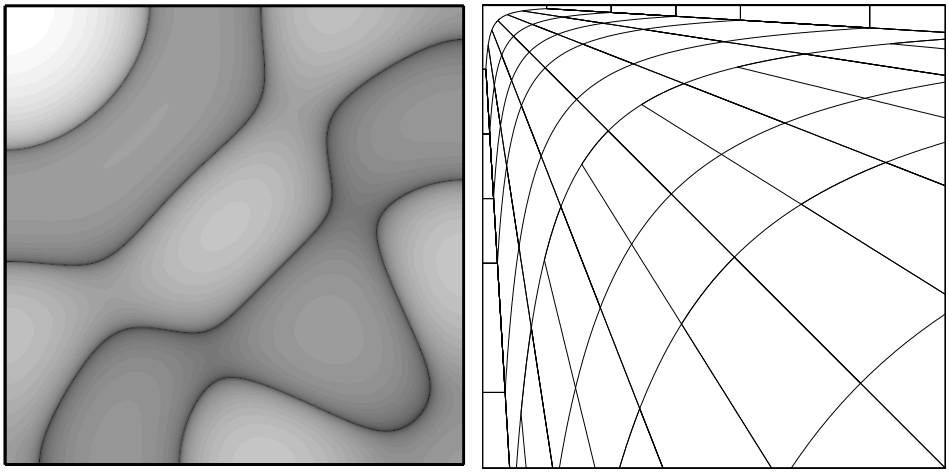

Fig. 22. The image on the left is the out-of-focus point spread function displayed in the DCT domain. The image on the right is the decomposition based on the hyperbolic composite wavelet when implemented by convolution with a reflexive boundary.

Table IV: Deconvolution results using the *Barbara* image.

$BSNR$	30	35	40	45
hyper	**25.90**	**27.41**	**29.09**	**31.12**
Tik	24.86	26.04	27.76	29.73

Our experiments emphasize the importance of having novel hyperbolic-based decompositions schemes for the problem of deconvolution. It si clear that there are other blurring functions that exhibit patterns containing valleys (low magnitude values) that follow a hyperbolic distribution. The point to make is that better regularization is possible when the image representation is sufficiently sparse, since it enables a superior control of the regularization parameters by isolating the locations of the valleys. A more complete study of this concept will be left to future work.

5 Conclusion

In this paper, we have demonstrated the potential of the framework of wavelets with composite dilations to construct and implement directional multiscale representations which are specifically designed to deal with edges and other anisotropic features with high efficiency. A new discrete method for decomposing images using this approach was devised that is much more flexible and sophisticated than previous design concepts. In fact, this new method succeeded to produce novel and useful constructions such as the hyperbolic decomposition. This was possible because our new filter bank construction follows directly from the generating structure. Not only does this design method follow faithfully from the theoretical framework, but it also enables one to obtain very sophisticate geometrical decompositions of the spatial frequency plane. Our new discrete transforms even improve upon the original implementation of the discrete shearlet transform, whose advantages in denoising and other imaging applications have been established in previous works. The numerical demonstrations included in this paper show that our new discrete transforms perform consistently better than similar directional multiscale transforms with respect to image denoising and enhancement.

References

[1] R. H. Bamberger and M. J. T. Smith, A filter bank for directional decomposition of images: theory and design, *IEEE Trans. Signal Process.*, 40(2), pp. 882–893, 1992.

[2] C. A. Berenstein, A. Yger, and B. A. Taylor, Sur quelques formules explicites de deconvolution, *Journal of Optics (Paris)* **14**, pp. 75–82, 1983.

[3] C. A. Berenstein, and A. Yger, Le problème de la déconvolution, *J. Funct. Anal.*, pp. 113–160, 1983.

[4] J. D. Blanchard, Minimally supported frequency composite dilation wavelets, *J. Fourier Anal. Appl.* 15 (2009), 796-815.

[5] J. D. Blanchard, Minimally Supported Frequency Composite Dilation Parseval Frame Wavelets, *J. Geom. Anal.* 19 (2009), 19-35.

[6] J. D. Blanchard and I. A. Krishtal, Matricial filters and crystallographic composite dilation wavelets, preprint (2010).

[7] E. J. Candès and D. L. Donoho, New tight frames of curvelets and optimal representations of objects with piecewise C^2 singularities, *Comm. Pure and Appl. Math.*, vol. 56, pp. 216–266, 2004.

[8] S. G. Chang, B. Yu, and M. Vetterli, Spatially adaptive wavelet thresholding with context modeling for image denoising, *IEEE Trans. on Imag. Processing*, vol. 9, no. 9, pp. 1522-1531, Sep. 2000.

[9] J. Chung, G. R. Easley, and D. P. O'Leary, Windowed Spectral Regularization of Inverse Problems, *preprint*, 2010.

[10] F. Colonna, and G. R. Easley, The multichannel deconvolution problem: a discrete analysis, *J. Fourier Anal. Appl.* **10**, pp. 351–376, 2004.

[11] A. L. Cunha, J. Zhou, M. N. Do, The nonsubsampled contourlet transform: Theory, design, and applications, *IEEE Trans. Image Processing*, **15**, pp. 3089–3101, 2006.

[12] M. N. Do and M. Vetterli, The contourlet transform: an efficient directional multiresolution image representation, *IEEE Trans. Image Process.*, vol. 14, no. 12, pp. 2091–2106, Dec. 2005.

[13] S. Durand, Orthonormal bases of non-separable wavelets with sharp directions, proc. of IEEE Int. Conf. on Image Proc., 2005.

[14] S. Durand, M-band filtering and non-redundant directional wavelets, Applied and Comput. Harmonic Analysis, 22(1):124-139, 2007.

[15] G. Easley, D. Labate, Critically sampled wavelets with composite dilations, to appear in *IEEE Trans. Image Process.* 2011.

[16] G. Easley, D. Labate and W. Lim, Sparse Directional Image Representations using the Discrete Shearlet Transform, *Appl. Comput. Harmon. Anal.* **25** pp. 25-46, (2008)

[17] G. R. Easley, and D. F. Walnut, Local multichannel deconvolution, *J. Math. Imaging Vision* **18**, pp. 69-80, 2003.

[18] K. Egan, Y-T Tseng, N. Holzschuch, F. Durand, R. Ramamorthi, Frequency Analysis and Sheared Reconstruction for Rendering Motion Blur, *ACM Transactions on Graphics*, vol. 28(3), pp. 93:1-13, 2009.

[19] R. Eslami and H. Radha, New image transforms using hybrid wavelets and directional filter banks: Analysis and design, *Proc. IEEE Int. Conf. Image Process. ICIP2005. Genova, Italy*, Sept. 2005.

[20] ——, Regular hybrid wavelets and directional filter banks: Extensions and applications, *Proc. IEEE Int. Conf. Image Process. ICIP2006. Atlanta, GA*, Oct. 2006.

[21] ——, A new family of nonredundant transforms using hybrid wavelets and directional filter banks, *IEEE Trans. Image Process.*, vol. 16, no. 4, pp. 1152–1167, April 2007.

[22] W. T. Freeman and E. H. Adelson, The design and use of steerable filters, *IEEE Trans. Patt. Anal. Mach. Intell.*, no. 9, pp. 891–906, September 1991.

[23] K. Guo and D. Labate, Optimally sparse multidimensional representation using shearlets, *SIAM J. Math. Anal.*, vol. 9, pp. 298–318, 2007.

[24] K. Guo, and D. Labate, Optimally Sparse 3D Approximations using Shearlet Representations, *Electronic Research Announcements in Mathematical Sciences*, **17** p. 126-138 (2010).

[25] K. Guo, D. Labate, W.-Q. Lim, D. Labate, G. Weiss, and E. Wilson, Wavelets with composite dilations, *Electron. Res. Announc. Amer. Math. Soc.*, vol. 10, pp. 78–87, 2004.

[26] ——, Wavelets with composite dilations and their MRA properties, *Appl. Comput. Harmon. Anal.*, vol. 20, pp. 220–236, 2006.

[27] ——, The theory of wavelets with composite dilations in: *Harmonic Analysis and Applications, C. Heil (ed.), pp. 231–249.* Boston, MA: Birkhäuser, 2006.

[28] G. Harikumar, and Y. Bresler, FIR perfect signal reconstruction from multiple convolutions: minimum deconvolver orders, *IEEE Transactions on Signal Proc.* **46**, pp. 215–218, 1998.

[29] J. Lu, D. M. Healy, Jr., Contrast enhancement via multi-scale gradient transformation, in *Wavelet Applications*, Proceedings of SPIE, Orlando, FL, April 5-8, 1994.

[30] S. Higaki, S. Kyochi, Y. Tanaka, and M. Ikehara, A novel design of critically sampled contourlet transform and its application to image coding, *Proc. IEEE Int. Conf. Image Process. ICIP2008. San Diego, CA*, Oct. 2008.

[31] I. Kryshtal, B. Robinson, G. Weiss, and E. Wilson, Compactly supported wavelets with composite dilations, *J. Geom. Anal.* **17** (2006), 87–96.

[32] G. Kutyniok and W.-Q Lim, Compactly supported shearlets are optimally sparse, *J. Approx. Theory*, to appear.

[33] D. Labate, W. Lim, G. Kutyniok, and G. Weiss, Sparse multidimensional representation using shearlets, Wavelets XI (San Diego, CA, 2005), 254–262, SPIE Proc. **5914**, SPIE, Bellingham, WA, 2005.

[34] A. F. Laine and X. Zong, A multiscale sub-octave wavelet transform for de-noising and enhancement, in *Wavelet Applications*, Proceedings of SPIE, Denver, CO, August 6-9, 1996, vol. 2825, pp. 238-249.

[35] S. Mallat, A Wavelet Tour of Signal Processing, Academic Press, San Diego, 1998.

[36] T. T. Nguyen and S. Oraintara, Multiresolution direction filterbanks: Theory, design, and applications, *IEEE Trans. Signal Process.*, **53**, no. 10, pp. 3895-3905, Oct. 2005.

[37] P. Schiske, Zur frage der bildrekonstruktion durch fokusreihen, *Proc. Eur. Reg. Conf. Electron. Microsc., 4th*, pp. 1–145, 1968.

[38] P. Schiske, Image processing using additional statistical information about the object. In P. W. Hawkes, ed., *Image Processing and Computer Aided Design in Electron Optics*. Academic Press, New York, 1973.

[39] E. P. Simoncelli and E. H. Adelson, Non-separable extensions of quadrature mirror filters to multiple dimensions, *Proceedings of the IEEE*, **78**, no. 4, pp. 652–664, April 1990.

[40] J. L. Starck, E. J. Candès, and D. L. Donoho, The curvelet transform for image denoising, *IEEE Trans Image Process.*, vol. 11, no. 6, pp. 670–684, 2002.

[41] J. L. Starck, F. Murtagh, E. Candes, and D. L. Donoho, Gray and Color Image Contrast Enhancement by the Curvelet Transform, *IEEE Trans. on Imag. Processing*, **12**, no. 6, pp. 706-717, June 2003.

[42] J. L. Starck, E. J. Candes, and D. L. Donoho, The Curvelet Transform for image denoising, *IEEE Trans. on Imag. Processing*, **11**, no. 6, pp. 670-684, June 2002.

[43] Y. Tanaka, M. Ikehara, and T. Q. Nguyen, Multiresolution image representation using combined 2D and 1D directional filter banks, *IEEE Trans. Image Process.*, no. 2, pp. 269–280, Feb. 2009.

[44] Z. Wang and A. C. Bovik, A universal image quality index, *IEEE Signal Processing Letters*, **9**, pp. 81-84, 2002.

[45] S. Yi, D. Labate, G. R. Easley, and H. Krim, *A Shearlet approach to Edge Analysis and Detection*, *IEEE Trans. Image Process* **18**(5) 929-941, (2009).

[46] J. Zhou, and M. N. Do, Multidimensional multichannel FIR deconvolution using Gröbner bases, *IEEE Trans. Image Proc.* **15**, pp. 2998–3007 , 2006.

6 Appendix

Below is a Matlab-based pseudo-code to generate the hyperbolic composite wavelet filters restricted to the fourth quadrant. The complete filters are found by adding the appropriate flip with zero padding. Let N_0 be the quadrant size of the image and $k \geq 2$ to be a multiplier to determine the number of sequence elements. Hr and Ht will denote the window functions for the radial and time parameters.

$N = kN_0$;
$k1 = 1/2$; $k2 = 1/k1$;
$r = \text{linspace}(k1, k2, N)$;
$t = \text{linspace}(2, 0, N)$;
$xs = [\,]$;$ys = [\,]$;
for $i = 1 : N$,
$x = \sqrt{r(i)}. * \lambda^t$;
$y = \sqrt{r(i)}. * \lambda^{-t}$;
$xs = [xs(:)'\, x(:)']$;
$ys = [ys(:)'\, y(:)']$;
end
for $j = j_0 : j_1$,
$$A_j = \begin{pmatrix} \sqrt{2}^j & 0 \\ 0 & \sqrt{2}^j \end{pmatrix};$$
for $l = l_0{:}l_1$,
$$B_l = \begin{pmatrix} \lambda^l & 0 \\ 0 & \lambda^{-l} \end{pmatrix};$$
$\eta = [xs(:)\ ys(:)](A_j B_l)$;
$\eta_1 = \eta(:, 1)$;$\eta_2 = \eta(:, 2)$;
$G = \text{zeros}(N_0)$;
$G_{weight} = \text{zeros}(N_0)$;
$c_i = 0$;
$c_{i_t} = 1$;
for $j_l = 1 : N$,
$\overline{\eta_1} = \lceil \eta_1(j_l) \rceil$;
$\overline{\eta_2} = \lceil \eta_2(j_l) \rceil$;
$c_i = c_i + 1$;
if $\overline{\eta_1} <= N_0$,
if $\overline{\eta_2} <= N_0$,
$G_{weight}(\overline{\eta_1}, \overline{\eta_2}) = G_{weight}(\overline{\eta_1}, \overline{\eta_2}) + 1$;
$G(\overline{\eta_1}, \overline{\eta_2}) = G(\overline{\eta_1}, \overline{\eta_2}) + Hr(c_i)Ht(c_{i_t})$;
end
end
if $c_i = N$,
$c_i = 0$;
$c_{i_t} = c_{i_t} + 1$;
end
if $c_{i_t} > N$
$c_{i_t} = 1$;
end
end

$\widehat{G}_{weight} = G_{weight}(1 : N_0, 1 : N_0);$
$\widehat{G} = G(1 : N_0, 1 : N_0);$
if $\|\widehat{G}\|_1 > 0$
$[i_0, j_0, nG] = \text{find}(\widehat{G}_{weight});$
$avg = 1./nG;$
$P = \text{sparse}(i_0, j_0, avg, N_0, N_0);$
$\widehat{G}_{i,l} = \widehat{G}. * P;$
end
end
end